Application of the Mechanical Threshold Stress Model to Large Strain Processing

Paul S. Follansbee

Professor Emeritus, Saint Vincent College, Latrobe, PA, USA
Email: paul.follansbee@stvincent.edu

Abstract

Large-strain deformations introduce several confounding factors that affect the application of the Mechanical Threshold Stress model. These include the decrease with the increasing stress of the normalized activation energy characterizing deformation kinetics, the tendency toward Stage IV hardening at high strains, and the influence of crystallographic texture. Minor additions to the Mechanical Threshold Stress model are introduced to account for variations of the activation energy and the addition of Stage IV hardening. Crystallographic texture cannot be modeled using an isotropic formulation, but some common trends when analyzing predominantly shear deformation followed by uniaxial deformation are described. Comparisons of model predictions with measurements in copper processed using Equal Channel Angular Pressing are described.

Keywords

Mechanical Threshold Stress Model, Large-Strain Deformations, ECAP, Stress-Strain Curves, Shear Deformations, Activation Energy, Strain-Hardening

1. Introduction

The Mechanical Threshold Stress (MTS) constitutive formalism is based on the definition of one or more internal state variables that characterize the interactions of dislocations with obstacle populations. The model was introduced because of the inability of common models, which included strain as a state parameter (or explicit model parameter) to follow path changes [1]. In the earliest application, the model was applied to the deformation of pure copper. In this case, dislocations interact solely with the evolving stored dislocation density, implying there is a single obstacle population; the governing constitutive equation is

$$\sigma = \sigma_a + s(\dot{\varepsilon}, T)\hat{\sigma} \tag{1}$$

where σ is the yield stress, σ_a is athermal stress, e.g., characterizing the interactions of dislocations with grain boundaries in a polycrystal, $\hat{\sigma}$ is the mechanical threshold stress and $s(\dot{\varepsilon}, T)$ is a kinetic factor, which varies between zero and unity according to the temperature T and strain rate $\dot{\varepsilon}$. The mechanical threshold stress is the yield stress at 0 K, where thermal activation does not assist the dislocation past the obstacle barrier. This equation specifies the yield stress σ for any "state". If this is a well-annealed copper material with a very low dislocation density, then $\hat{\sigma}$ is zero and σ simply equals σ_a. If, instead, this is a material that has been deformed according to some strain rate and temperature path to a strain ε, then $\hat{\sigma}$ is non-zero, and σ represents the yield stress when this material is further strained at the temperature T and strain rate $\dot{\varepsilon}$ specified in Equation (1).

Equation (1) is a simplified correlation between the yield stress and threshold stress. It is sensible to normalize stress by the temperature-dependent shear modulus to remove this contribution to $s(\dot{\varepsilon}, T)$, giving

$$\frac{\sigma}{\mu(T)} = \frac{\sigma_a}{\mu(T)} + s(\dot{\varepsilon}, T)\frac{\hat{\sigma}}{\mu_0(T)} \tag{2}$$

The kinetic factor $s(\dot{\varepsilon}, T)$ specifies how the thermal activation assists stress to enable a dislocation to overcome an obstacle—in this case another dislocation, either part of the stored dislocation density or on an alternate slip system. One correlation for s is [2] [3]

$$s(\dot{\varepsilon}, T) = \left[1 - \frac{kT}{G}\ln\left(\frac{\dot{\varepsilon}_o}{\dot{\varepsilon}}\right) \right] \tag{3}$$

where G is the activation energy, k is Boltzmann's constant, and $\dot{\varepsilon}_o$ is a constant. A more rigorous form of Equation (3), which normalizes G by μb^3 and accounts for a more realistic obstacle profile is [2]

$$s(\dot{\varepsilon}, T) = \left\{ 1 - \left[\frac{kT}{g_o \mu b^3}\ln\left(\frac{\dot{\varepsilon}_o}{\dot{\varepsilon}}\right) \right]^{1/q} \right\}^{1/p} \tag{4}$$

where g_o is the normalized activation energy, and p and q are constants. Combining Equation with Equation (2) and rearranging gives

$$\left(\frac{\sigma - \sigma_a}{\mu}\right)^p = \left\{ 1 - \left[\frac{kT}{g_o \mu b^3}\ln\left(\frac{\dot{\varepsilon}_o}{\dot{\varepsilon}}\right) \right]^{1/q} \right\}\left(\frac{\hat{\sigma}}{\mu_o}\right)^p \tag{5}$$

Figure 1 gives an example of how this analysis is applied in deformed copper [4]. In this experiment, copper compression specimens (at least 8) were "prestrained" at room temperature and strain rates specified to the true strain specified (e.g., $\dot{\varepsilon}$ = 0.82 s^{-1} to ε = 0.727). The specimens were then "reloaded" at various temperatures and strain rates. This plot shows four sets of reload yield stress as a function of reload temperature and strain rate. The dashed lines are drawn according to Equation (5) with σ_a = 40 MPa, p = 2/3, q = 1, and $\dot{\varepsilon}_o$ = 10^7 s^{-1}.
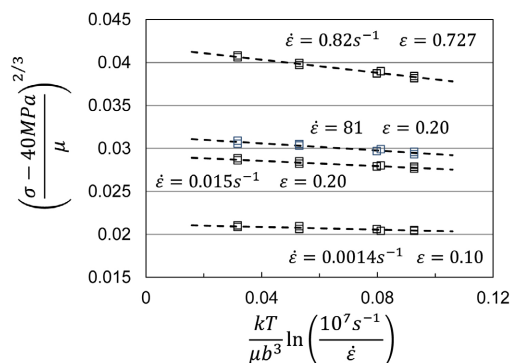
Figure 1. Reload yield stress versus reload strain rate and temperature for four prestrain conditions.

The temperature-dependent shear modulus are defined according to a correlation proposed by Varshni [5]

$$\mu(T) = \mu_o - \frac{D_0}{\exp\left(\dfrac{T_0}{T}\right) - 1} \tag{6}$$

where μ_o is the shear modulus at 0 K and D_0 and T_0 are constants. The intercept at an abscissa value of zero gives $\hat{\sigma}$ while the normalized activation energy g_o is related to the slope of each dashed line. Table 1 gives a summary of these values for the four prestrain conditions.

In the original Follansbee and Kocks study [4], there were actually 41 prestrain conditions, including the four shown in **Figure 1** and tabulated in **Table 1**. One curious result of this work was a subtle but systematic variation of the normalized activation energy with $\hat{\sigma}$. This is evident in **Table 1**, where a threshold stress increase from 141 MPa to 392 MPa yields a decrease in the normalized activation energy from 2.7 to 1.1. **Figure 2** shows the full set of results for all of the prestrain conditions. Although there is a lot of scatter in the measurements, particularly at low values of the threshold stress, the trend is evident.

The variation of the normalized activation energy was ignored in early MTS model applications [3] and an average value of g_0 equals 1.6 was selected. This is an acceptable approximation when the strain range is small, e.g., in a typical tensile test. However, recently there has been increasing attention on very large deformations, in order, for instance, to refine the grain size [6] [7]. The total strains of interest can exceed 5. In this case, the decrease of g_0 with increasing deformation should not be ignored. The objective of this manuscript is to introduce a model that accounts for this dependence. Model predictions are compared to large-strain deformation measurements. Particular interests are the measured and predicted strain-rate sensitivities.

2. Stress Dependence of the Normalized Activation Energy

In their analysis of measurements in silver single crystals and copper polycrystals, Mecking and Kocks [8] noted an increase of $s(\dot{\varepsilon}, T)$ with increasing stress.
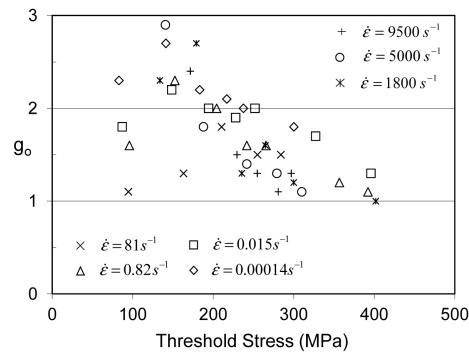
Figure 2. Normalized activation energy versus stress for all prestrain conditions.

Table 1. Variation of the Mechanical Threshold Stress and the normalized activation energy for the four prestrain conditions illustrated in **Figure 1**.

Prestrain, 295 K		$\hat{\sigma}$, MPa	g_0
$\dot{\varepsilon}$, s^{-1}	ε		
0.82	0.727	392	1.1
81	0.20	255	1.5
0.015	0.20	228	1.9
0.00014	0.10	141	2.7

They characterized this as deviation from the Cottrell-Stokes law and proposed a phenomenological model for the strain-rate sensitivity, $m \times s$, where m is defined

$$m = \left. \frac{\partial \ln \sigma}{\partial \ln \dot{\varepsilon}} \right|_{\varepsilon, T} \tag{7}$$

Mecking and Kocks proposed

$$\left. \frac{\partial \sigma}{\partial \ln \dot{\varepsilon}} \right|_{T, \hat{\sigma}} = \frac{\sigma}{r_o} \left(1 + \frac{r_o}{n} F \frac{\theta_r}{\theta_h} \right) \tag{8}$$

where n and F are constants, and θ_r and θ_h represent the "recovery" and "hardening" contributions to strain hardening. The variable r_o in Equation (8) is related to the strain-rate sensitivity of $s(\dot{\varepsilon}, T)$

$$r = \left. \frac{\partial \ln \dot{\varepsilon}}{\partial \ln s} \right|_T \tag{9}$$

and r_o is the value of r at low stresses (where Cottrell-Stokes is obeyed).

Strain hardening in the Mechanical Threshold Stress deformation model treats evolution of the mechanical threshold stress with the Voce Law [9]. The law considers the balance between the recovery and hardening contributions to strain hardening:

$$\frac{\mathrm{d}\hat{\sigma}_{\varepsilon}}{\mathrm{d}\varepsilon} = \theta_{II} \left[1 - \frac{\hat{\sigma}_{\varepsilon}}{\hat{\sigma}_{\varepsilon s}(\dot{\varepsilon}, T)} \right] = \theta_{II} - \frac{\theta_{II} \hat{\sigma}_{\varepsilon}}{\hat{\sigma}_{\varepsilon s}(\dot{\varepsilon}, T)} = \theta_h - \theta_r \tag{10}$$

where θ_{II} is the stage II hardening rate (equals θ_h) and $\hat{\sigma}_{\varepsilon s}(\dot{\varepsilon}, T)$ is the saturation value of the mechanical threshold stress. The ratio of the recovery term to the hardening term becomes

$$\frac{\theta_r}{\theta_h} = \frac{\hat{\sigma}_\varepsilon}{\hat{\sigma}_{\varepsilon s}(\dot{\varepsilon}, T)} \tag{11}$$

Equation (8) with Equation (11) suggests that the strain-rate sensitivity rises as θ_r approaches θ_h (or equivalently as $\hat{\sigma}_\varepsilon$ approaches $\hat{\sigma}_{\varepsilon s}$). Starting with a simplified version of Equation (5) (with $p = q = 1$ and without normalizing by the temperature-dependent shear modulus to simplify the analysis),

$$\sigma = \sigma_a + \left[1 - \frac{kT}{\mu b^3 g_{o\varepsilon}} \ln \frac{\dot{\varepsilon}_o}{\dot{\varepsilon}}\right]\hat{\sigma}_\varepsilon \tag{12}$$

it can be shown that

$$r_o = \frac{\partial \ln \dot{\varepsilon}}{\partial \ln s} = \frac{\mu b^3 g_{o\varepsilon_o}}{kT} - \ln \frac{\dot{\varepsilon}_o}{\dot{\varepsilon}} \tag{13}$$

Note in Equation (12) that the normalized activation energy in Equation (5) (g_0), and been replaced by $g_{0\varepsilon}$ to emphasize that this activation energy arises from the interaction of dislocations with stored dislocations and that it evolves with stress. The constant $g_{o\varepsilon_o}$ is the value of $g_{o\varepsilon}$ when the Cottrell-Stokes law is obeyed,

$$\left.\frac{\partial \sigma}{\partial \ln \dot{\varepsilon}}\right|_{T,\hat{\sigma}} = \frac{kT}{\mu b^3 g_{o\varepsilon}}\hat{\sigma}_\varepsilon \tag{14}$$

Combining Equation (8) and Equation (14) and rearranging gives

$$g_{o\varepsilon} = \frac{kT}{\mu b^3}\frac{r_o}{\sigma}\left(\frac{1}{\dfrac{1}{\hat{\sigma}_\varepsilon} + \dfrac{r_o}{n} F \dfrac{1}{\hat{\sigma}_{\varepsilon s}}}\right) \tag{15}$$

Equation (15) specifies that as $\hat{\sigma}_\varepsilon$ rises, $g_{0\varepsilon}$ falls—as observed in **Figure 2**. It is possible to fit Equation (15) to the Follansbee and Kocks measurements in copper. This equation, however, is not very robust—particularly at low strains in annealed material where $\hat{\sigma}_\varepsilon$ is initially zero and σ can also be very low. Accordingly, the following, somewhat related, expression is adopted

$$g_{o\varepsilon} = \frac{kT}{\mu b^3}r_o\left(\frac{1}{1 + F\dfrac{\hat{\sigma}_\varepsilon}{\hat{\sigma}_{\varepsilon s}}}\right) \tag{16}$$

This expression also uses r_o (Equation (13)) as an initial condition—even though this was not evaluated for a fully rigorous yield stress equation, e.g., Equation (5). Combining Equation (13) with Equation (16) gives

$$g_{o\varepsilon} = \left(g_{o\varepsilon_o} - \frac{kT}{\mu b^3}\ln\left(\frac{\dot{\varepsilon}_o}{\dot{\varepsilon}}\right)\right)\left(\frac{1}{1 + F\dfrac{\hat{\sigma}_\varepsilon}{\hat{\sigma}_{\varepsilon s}}}\right) \tag{17}$$

According to Equation (17), $g_{o\varepsilon}$ starts at the (high) initial value when $\hat{\sigma}_\varepsilon$ is low but decreases with increasing $\hat{\sigma}_\varepsilon$. **Figure 3** gives the measured $g_{o\varepsilon}$ versus the value predicted from Equation (17). It should be noted that the strain rate used in the calculation of the factor r_o (Equation (13)) is a typical reload strain rate rather than the prestrain strain rate used to differentiate data points in **Figure 3**. The dashed line is the fit to Equation (17) (excluding the five data points at the lowest values of strain for each of the strain rates because they deviate from the linear behavior). The line has a slope of unity and intercepts at the origin. The factor F in Equation (17) has a value $F = 3.16$ and $g_{o\varepsilon_0} = 4.7$. Although considerable scatter is evident in **Figure 3** the trends follow the behavior modeled using Equation (17).

Alberti [10] measured the strain-rate sensitivity in polycrystalline copper strained to very high strains in torsion. **Figure 4** compares the Alberti measurements (after converting from shear stress to axial stress) and model predictions of m-value using Equation (14) with Equation (17). The model predictions closely follow the Alberti measurements.

3. Stress-Strain Predictions at Large Strains

The objective of this section is to model large-strain deformation. In particular, the model should be able to describe the strain-rate sensitivity in a material
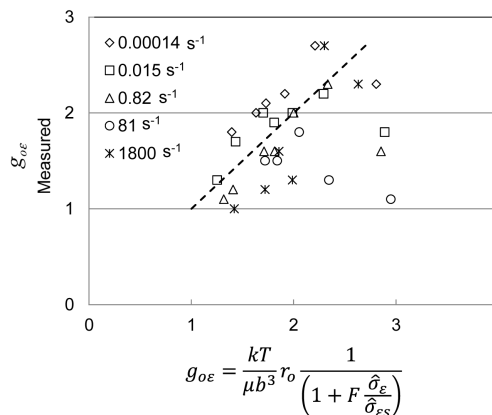

$$g_{o\varepsilon} = \frac{kT}{\mu b^3} r_o \frac{1}{\left(1 + F \frac{\hat{\sigma}_\varepsilon}{\hat{\sigma}_{\varepsilon s}}\right)}$$

Figure 3. Fit of Equation (17) to the data plotted in **Figure 2**.
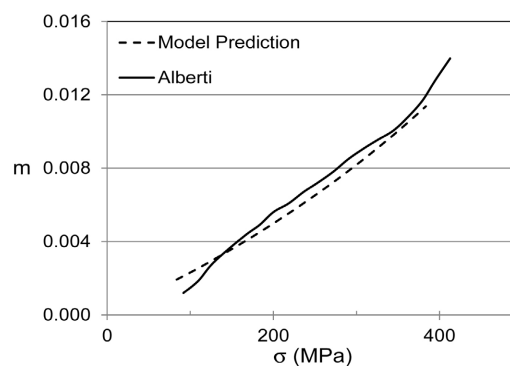

Figure 4. Fit of Equation (17) to strain-rate sensitivity measurements by Alberti [10].

processed to large strains. One of the requirements for such a model is to include the variation of the normalized activation energy with increasing stress. This correlation was developed in the previous section. Another requirement is to have access to stress-strain curves deformed to large strains (e.g., $\varepsilon > 2$). The strains achieved in a tensile test rarely exceed 0.5 due to necking. Compression tests, when carefully performed to minimize barreling, or torsion tests, however, are able to achieve these strain levels.

Figure 5 shows the large strain measurements of Kocks *et al.* [11] in copper at room temperature and a strain rate of 0.001 s^{-1}. Included are stress-strain curves (von Mises' stress versus von Mises' strain) measured in compression and torsion[1]. One notable observation in **Figure 5** is that the two curves do not coincide —even when plotted on von Mises' coordinates that are designed to account for differences in a stress state. The reason for this is that texture evolution differs in a uniaxial test from that in a torsion test. Another observation in **Figure 5** is that above a strain of ~1 both the compression and torsion curves demonstrate an almost linear strain-hardening rate, deviating from the approach to saturation stress modeled using the standard evolution law (Equation (10)). This behavior has been termed "Stage IV" hardening [12].

Figure 6 compares the measured and predicted compression stress-strain curves. The predicted curve is with Equation (5), Equation (6), and a slightly modified version of Equation (10):
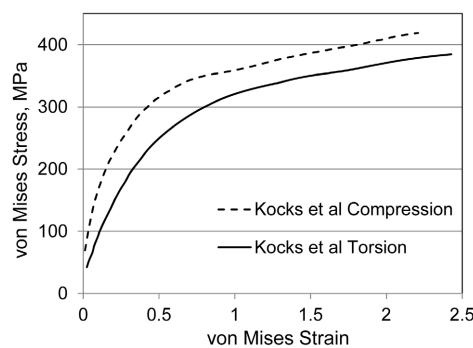

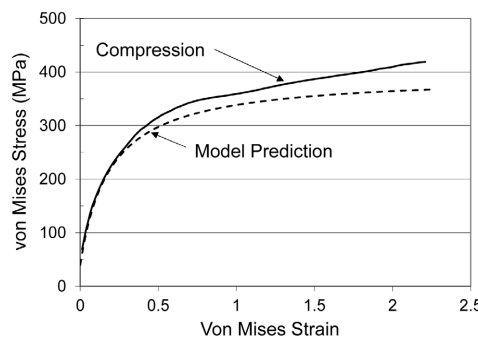**Figure 5.** Large strain stress-strain curves measured in copper by Kocks *et al.* [11].

Figure 6. Model prediction for the large-strain comression curve.

---

[1]Recall that von Mises' stress and strain are equivalent to uniaxial stress and strain in a tension or compression test.

$$\frac{\mathrm{d}\hat{\sigma}_\varepsilon}{\mathrm{d}\varepsilon} = \theta_{II}\left(\dot{\varepsilon}\right)\left(1 - \frac{\hat{\sigma}_\varepsilon}{\hat{\sigma}_{\varepsilon s}\left(\dot{\varepsilon},T\right)}\right)^{\kappa} \tag{18}$$

where the term on the right-hand side of the Voce law is raised to the power k. A value of $k = 2$ provides a better fit to the hardening measurements than does a value of $k = 1$. The parameter θ_{II} in Equation (18) has a slight strain rate dependence:

$$\theta_{II} = A_0 + A_1 \ln \dot{\varepsilon} + A_2 \sqrt{\dot{\varepsilon}} \tag{19}$$

where A_0, A_1, and A_2 are constants. For the parameter $\hat{\sigma}_{\varepsilon s}\left(\dot{\varepsilon},T\right)$, the dynamic recovery model proposed by Kocks [13] is used:

$$\ln \hat{\sigma}_{\varepsilon s} = \ln\left(\hat{\sigma}_{\varepsilon so}\right) + \frac{kT}{\mu b^3 \left(g_{\varepsilon so}\right)} \ln \frac{\dot{\varepsilon}}{\dot{\varepsilon}_{\varepsilon so}} \tag{20}$$

where k is Boltzmann's constant, μ is the shear modulus (Equation (6)), b is the Burgers vector, and $\hat{\sigma}_{\varepsilon so}$, $g_{\varepsilon so}$, and $\dot{\varepsilon}_{\varepsilon so}$ are constants. The model constants in these equations were derived for 0.9999 Cu [3] and are listed in Table 2.

Note in this basic model, the normalized activation energy in Equation (5) is taken as the constant value of 1.6 rather than the stress-dependent value described in the previous section and specified by Equation (17). Comparison of

Table 2. Model parameters for the predictions of Figures 6-8.

Equation	Parameter	Value		
		Figure 6	Figure 7	Figure 8
5	σ_a (MPa)		40	
	p		2/3	
	q		1	
	$\dot{\varepsilon}_{o\varepsilon}$ (s⁻¹)		10^7	
	$g_{o\varepsilon}$	1.6	-	
20	$\hat{\sigma}_{\varepsilon so}$ (MPa)	710	740	760
	$\dot{\varepsilon}_{\varepsilon so}$ (s⁻¹)		10^8	
	$g_{\varepsilon so}$		0.301	
21	κ		2	
	θ_{IV} (MPa)	-	75	50
19	A_0 (MPa)	2390	2390	1120
	A_1^a		12.0	
	A_2 (s⁻¹)		1.696	
17	$g_{o\varepsilon_0}$	-		4.7
	F	-		3.16

aThe units of A_1 are awkward since A_1 multiplies the natural logarithm of $\dot{\varepsilon}$ (s⁻¹).

the measured and predicted stress-strain curves in Figure 6 highlights the inability of the hardening law (Equation (18)) to accurately describe the hardening at strains exceeding ~0.4. The predicted curve converges toward a saturation stress whereas the measurement demonstrates continued hardening (Stage IV) [12].

One simple way to include Stage IV hardening in the evolution law is to add a linear hardening term to Equation (18)

$$\frac{d\hat{\sigma}_{\varepsilon}}{d\varepsilon} = \theta_{II}\left(\dot{\varepsilon}\right)\left(1 - \frac{\hat{\sigma}_{\varepsilon}}{\hat{\sigma}_{\varepsilon s}\left(\dot{\varepsilon}, T\right)}\right)^{\kappa} + \theta_{IV} \tag{21}$$

where θ_{IV} is a constant. Equation (21) is applicable when $\hat{\sigma}_{\varepsilon} \leq \hat{\sigma}_{\varepsilon s}$. When $\hat{\sigma}_{\varepsilon} > \hat{\sigma}_{\varepsilon s}$, the evolution law is simply

$$\frac{d\hat{\sigma}_{\varepsilon}}{d\varepsilon} = \theta_{IV} \tag{22}$$

Figure 7 shows the comparison of the measured compression stress-strain curve with the prediction when Equation (17) is applied for the variation of $g_{o\varepsilon}$ with stress and when Equation (21) is used for the hardening law. The model variables for this prediction are also included in Table 2. Most have not changed from the values used in the prediction in Figure 6; a few (e.g., $\hat{\sigma}_{\varepsilon so}$ and A_0) changed slightly. The measured and predicted curves in Figure 7 agree closely.

In order to use the constitutive equations described above to analyze copper that has been Equal Channel Angular Pressing (ECAP) processed (see next section), there is one additional factor to be addressed. The strains imposed in ECAP as the billet makes the turn (usually 90°) through the die are largely shear strains. Figure 7 demonstrates the application of the model to the compression test result shown in Figure 5. This figure, however, included a test in torsion, and it already has been emphasized that the stress levels in this test—even when plotted on von Mises stress and strain coordinates—are less than those observed in compression. The analysis described for the predicted stress-strain curve in Figure 7 can be reapplied to the torsion stress-strain curve. Figure 8 compares the measured and predicted stress-strain curves. The column labeled "Figure 8" in Table 2 lists the model parameters used to generate the predicted stress-strain
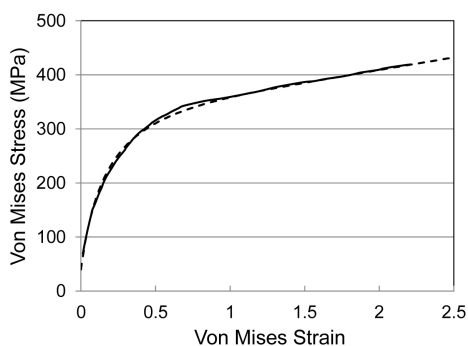

Figure 7. Model predidtion (dashed line) for the large-strain comression curve with the inclusion of Stage IV hardening.
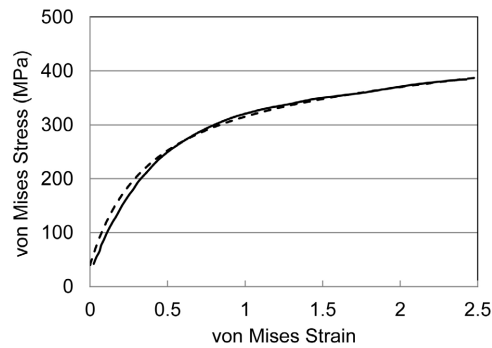
Figure 8. Model predidtion (dashed line) for the large-strain torsion curve with the inclusion of Stage IV hardening.

curve. The most significant change in model parameters is the decrease of A_0 (Equation (19)) from 2390 MPa (for **Figure 8**) to 1120 MPa. The model prediction over-estimates the measured stress levels at low strains, but agrees well with the measured stress levels to the maximum strain of 2.5.

4. Application to ECAP Processed Copper

One experimental method used to achieve large deformations is Equal Channel Angular Pressing (ECAP) where a billet is forced through a die with a high (often 90˚) included angle. A schematic of such a die is shown in **Figure 9**. When the angle is 90˚, one pressing through such a die produces a strain of 1.15.

Dalla Torre *et al.* [14] measured the reload stress-strain and strain-rate sensitivity behavior on 99.95% pure copper with a starting grain size of 21 μm deformed using 90˚ ECAP and 1, 2, 4, 8, 12, and 16 pressings. The equations developed in the previous sections may be used to predict the stress-strain behavior during deformation along with the stress-strain curve and strain-rate sensitivity upon reloading. Because this material was not as pure as the Follansbee and Kocks material and had a slightly smaller initial grain size, the governing equation (Equation (5)) is revised. In particular, the athermal stress is taken as 60 MPa to reflect the slightly smaller grain, and an impurity obstacle ($\hat{\sigma}_i$) of 46 MPa is assumed to reflect the lower purity level. That is, Equation (5) becomes

$$\frac{\sigma}{\mu} = \frac{60\,\text{MPa}}{\mu} + \left\{1 - \frac{kT}{\mu b^3 g_{o\varepsilon}\left(\hat{\sigma}_\varepsilon\right)}\ln\frac{10^7\,\text{s}^{-1}}{\dot{\varepsilon}}\right\}^{3/2}\frac{\hat{\sigma}_\varepsilon}{\mu_o} + s_i\left(\dot{\varepsilon},T\right)\frac{\hat{\sigma}_i}{\mu_o} \qquad (24)$$

where s_i is as specified in Equation (4) with $g_{oi} = 0.6$, which is a typical normalized activation energy for an impurity obstacle population [3], $\hat{\sigma}_i$ = 46 MPa, p_i = 0.5, q_i = 1.5, and $\dot{\varepsilon}_{oi}$ = 10^7 s^{-1}. The applicable equations become Equation (24), Equation (17), and Equation (21) (with Equation (19) and Equation (20)). All other model constants listed in **Table 2** remain the same for the predictions.

Figure 10 shows the predicted stress-strain curve (dashed line) during the first pressing and the measured (solid line) and predicted RT reload stress-strain curve at a strain rate of 0.001 s^{-1}. Included in this figure are the measured and predicted strain-rate sensitivities (right abscissa) at several values of strain
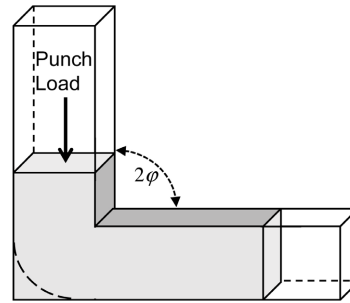
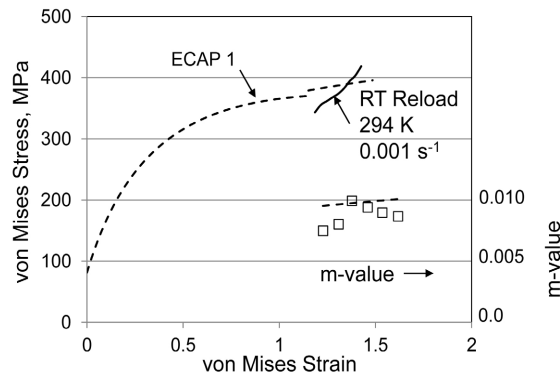**Figure 9.** Typical equal channel angular pressing die.

Figure 10. Predicted and measured reload and rate sensitivity for 1 ECAP pressing.

during the reload operation. In these experiments the 20 mm long work piece was fed at a velocity of 2 mm/s. If this were uniform loading, these variables would imply a strain rate of 0.1 s^{-1}. Given that deformation is localized in the region near the bend, the applicable strain rate is likely at least 1 s^{-1}, which has been assumed in making the model predictions. This strain rate is at the transition to an adiabatic condition, which implies that the temperature rises during the pressing. For this test, the temperature is estimated to rise from the starting temperature of 294 K to a final temperature of 388 K at the final strain of 1.15, computed using

$$\Delta T = \frac{\psi}{\rho c_p} \int \sigma \mathrm{d}\varepsilon \qquad (25)$$

where ψ, the fraction of energy converted to heat [3], is assumed to equal 0.95. The measured reload yield stresses fall somewhat below the predicted values and the measured rate strain hardening during the reload exceeds the predicted rate. The predicted stresses upon reload differ from the stress level achieved during ECAP processing because the temperature returns to room temperature and the strain rate decreases to 0.001 s^{-1}. The model predictions show a uniform increase of m-value with strain; the measurements show similar values but exhibit more scatter.

Figure 11 shows the predicted reload stress-strain curve and strain-rate sensitivity after the second ECAP pressing. In this case, the strain starts at 1.15; the final total strain due to the first and second pressings is 2.30. Note that the
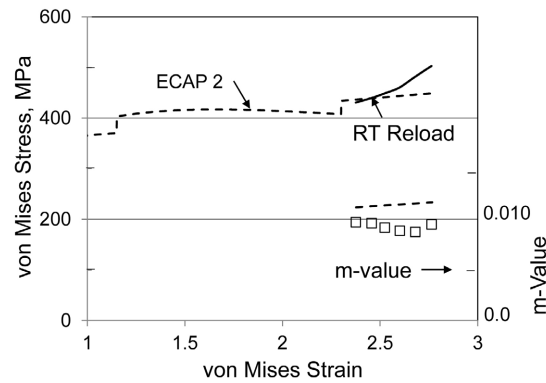
Figure 11. Predicted and measured reload and rate sensitivity for 2 ECAP pressings.

temperature at the start of the second pressing as well as at the start of the reload is reduced to room temperature The predicted reload yield stress is close to the measured value, the measured strain hardening exceeds the predicted strain hardening, and the predicted strain-rate sensitivity is greater than the measured strain-rate sensitivity.

Figure 12 shows the measurement and prediction after the third and fourth pressings. The strain during these pressings increases from 2.30 to 4.60. It should be emphasized that the measured stress-strain curve in torsion (Figure 5) only went to a strain of ~2.4. Equation (21) is used beyond this strain, which implies that the Stage IV hardening observed is assumed to proceed to strains almost twice as large. This may well be a source of error in the predictions. The trends in the comparison between the measurement and prediction mirror those observed after the first and after the second pressings, in that the predicted rate of strain hardening is low and the strain-rate sensitivity is fairly well-predicted, although there is considerable scatter observed in the measurements. Note, however, that the predicted reload yield stress is quite high.

The comparison between the measured and predicted stress-strain curves after one ECAP pressing in Figure 10 indicated that the reload yield stress was over-predicted. From Equation (24) the term that contributes to this over-prediction is $\hat{\sigma}_\varepsilon$, which was computed integrating Equation (21) as the billet is strained to a strain of 1.15 at 1.0 s^{-1} and a temperature that increases during straining due to adiabatic heating. This calculation leads to a value of $\hat{\sigma}_\varepsilon$ at the end of one ECAP pressing (and, thus, the start of the reload) of 371 MPa. To estimate how much $\hat{\sigma}_\varepsilon$ is overestimated, one can find the value of $\hat{\sigma}_\varepsilon$ that leads to agreement between the measured and predicted reload yield stress. Figure 13 shows the measured and predicted reload stress-strain curve when $\hat{\sigma}_\varepsilon$ is set at 325 MPa, suggesting that the predicted value of $\hat{\sigma}_\varepsilon$ is overestimated by 46 MPa. Note that the predicted rate of strain hardening remains high. However, the measured and predicted strain-rate sensitivities (m-value) agree more closely in Figure 13 (with $\hat{\sigma}_\varepsilon$ = 325 MPa) than in Figure 10 (with $\hat{\sigma}_\varepsilon$ = 371 MPa). Given the dependence of the $g_{o\varepsilon}$ (which contributes to the m-value) on the stress level defined by Equation (17), this improved agreement is sensible.
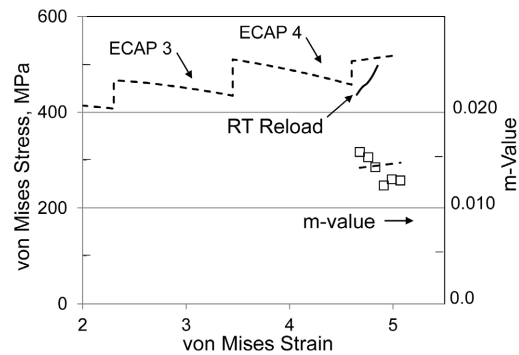
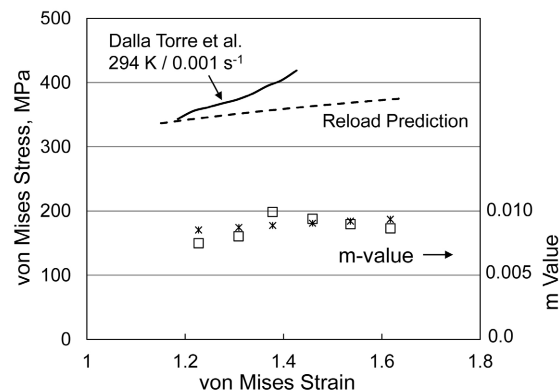**Figure 12.** Predicted and measured reload and rate sensitivity for after 4 ECAP pressings.

Figure 13. Predicted and measured reload and rate sensitivity after 1 ECAP pressing when threshold stress at start of the reload set to 325 MPa (instead of the predicted 371 MPa).

Figure 14 shows the same comparison of measured and predicted stress-strain curves and strain-rate sensitivities after four ECAP pressings. In this case, the strain plotted is the strain during the reload; the total strain is the strain shown plus the total ECAP strain of 4.6. In order to achieve agreement between the measured and predicted yield stresses, $\hat{\sigma}_\varepsilon$ is set at 472 MPa, which is 115 MPa less than the value predicted using Equation (21).

Figure 15 compiles these estimates through eight ECAP pressings. The open triangles are the values of $\hat{\sigma}_\varepsilon$ predicted using Equation (21), whereas the open boxes are the values established by forcing agreement of the predicted and reload yield stresses. As shown in Figure 13, the predicted and estimated values agree fairly well up through two ECAP pressings. The difference, however, rises after the second, fourth, and eighth pressings. In fact, Figure 15 shows that there is almost no increase in $\hat{\sigma}_\varepsilon$ from the fourth through the eighth ECAP pressings (only 18 MPa).

5. Discussion

There are essentially two possible explanations for the apparent saturation of hardening as strains exceed 2. One is that dynamic recrystallization is active. The second is that the hardening law expressed by Equation (21) is inaccurate. With
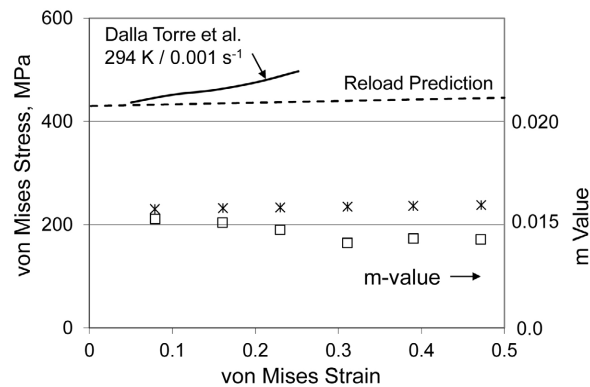
Figure 14. Predicted and measured reload and rate sensitivity after 4 ECAP pressings when threshold stress at start of the reload set to 472 MPa (instead of the predicted 587 MPa).
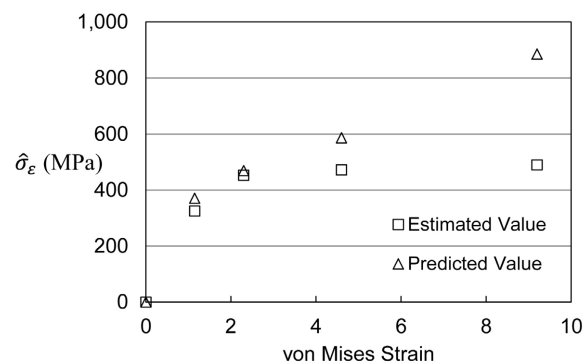

Figure 15. Predicted and estimated threshold stress at the start of the reload for 1 through 8 ECAP pressings, showing that strain hardening appears to saturate.

regard to the possibility for dynamic recrystallization, it was estimated earlier that during the first ECAP pressing, the adiabatic temperature rise increased the temperature to 388 K. This estimate assumes uniform straining across the billet cross-section. If, as expected, local strains in the vicinity of the corner in the ECAP die are higher, this temperature could certainly increase. Zhang *et al.* measured grain size and the stored energy in ECAP processed 0.9998 copper with an initial grain size of 100 μm [15]. They reported grain size reductions that leveled out at a grain size of ~0.26 μm after total strains of ~10. The stored energy increases with increasing strain, but, along with the grain size, the stored energy saturates at a strain of ~10. **Figure 16** shows the increase of $\hat{\sigma}_\varepsilon$ and increase of the stored energy with strain (left ordinate) measured by Zhang *et al.* Included in **Figure 16** is the decrease of grain size with strain (right ordinate). The trends mirror each other. Importantly, the minimum recrystallization temperature estimated by Zhang *et al.* is on the order of 480 K. Based on these measurements, it seems as if recrystallization is not the dominant contributing factor to the lower rates of strain hardening observed in ECAP processed copper.

The alternate explanation for the low rate of strain hardening was that Equation (21) over-predicted the rate of strain hardening. In **Figure 8** this equation
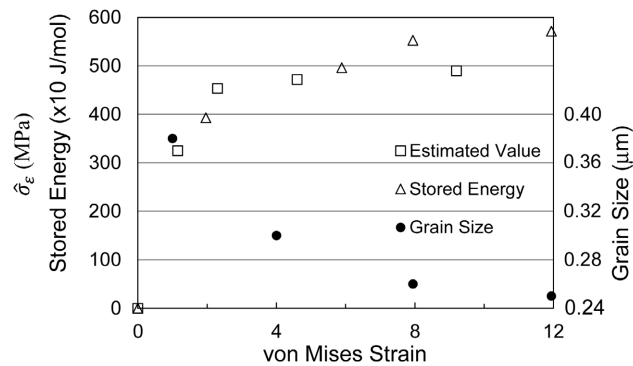
Figure 16. Measured grain size and stored energy in ECAP processed copper by Zhang *et al.* [15] compared to estimated threshold stresses.

was fit to the large-strain torsion test shown in **Figure 5**, which involved strains as high as 2.43. The strain after two ECAP pressings is 2.30. Thus, one would expect that stress predictions at strain as high as 2.4 would be accurate, but that predictions at higher strains would require extrapolations. The comparison of estimated and predicted values of $\hat{\sigma}_\varepsilon$ in **Figure 15** validates the suspicion that the extrapolation of Equation (21) to higher strains of ~2.4 is dangerous. That is, Stage IV hardening represented by a constant value of θ_{IV} (Equation (21)) at higher strains does not appear to be warranted.

A common observation in the reload stress-strain curves following one ECAP pressing (**Figure 10**), two ECAP pressings (**Figure 11**), four ECAP pressings (**Figure 12**) and eight ECAP pressings (**Figure 13**) is the higher than predicted rate of strain hardening. Insight into the potential influence of the stress-path change in transitioning from a predominantly shear stress state during ECAP processing to a uniaxial stress-state during tension or compression reload testing is gained from large-strain measurements in 304 L stainless steel by Miller and McDowell [16]. In addition to measuring stress-strain curves using pure torsion and pure compression stress states, these investigators studied the response of tubes strained in torsion to effective (or von Mises) strain levels of 0.5 and 1.0 followed by tension. (Note that Miller and McDowell report that torsion followed by compression was not possible due to plastic instability in the compression specimen.)

Figure 17 shows the result for a prestrain of 1.0 at a strain rate of 0.0004 s^{-1} followed by tension at the same strain rate. In this case, the reload tension test shows yield at nearly the same von Mises stress level as observed in the torsion test, but the rate of strain hardening is very high. This behavior is reminiscent of the compression reload results showing copper in **Figure 10** and **Figure 13**. It is suggested that a high reload strain hardening rate is a texture effect and that the softer texture formed during shear transforms upon reloading to a texture consistent with a uniaxial stress state, which is a stronger configuration. Since ECAP is a predominantly shear deformation process, the expectation is that high strain hardening in a uniaxial reload test should be commonly observed.
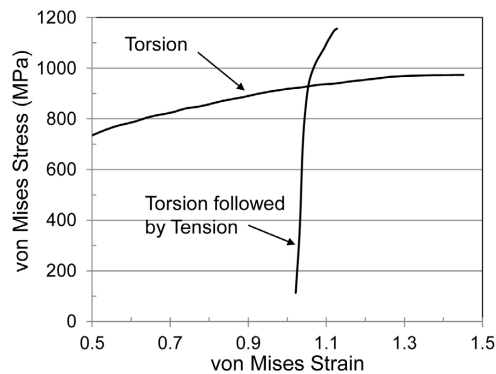
Figure 17. Torsion followed by tension in 304 L stainless steel measured by measured grain size and stored energy in ECAP processed copper by Miller and McDowell [16].

6. Conclusions

Predictions of stress-strain curves and strain-rate sensitivities on material deformed to large strains require a model for the decrease of the normalized activation energy with increasing stress. Following the work of Mecking and Kocks, Equation (17) was derived. This simple addition to the MTS formalism was shown to describe the variation of the strain-rate sensitivity with stress.

Another requirement for large-strain predictions is an evolution equation that includes the effects of Stage IV hardening observed in large strain measurements. Equation (21) was consistent with measurements in compression and torsion to strains as high as 2.4. Analysis of ECAP processed copper at even higher strains led to the conclusion that Equation (21) over-predicts strain hardening when strains rose above ~2.4.

Comparison with calorimetry and grain-size measurements in ECAP processed copper suggests that recrystallization is not strongly affecting the rate of strain hardening at strain levels as high as 10.

The analysis of stress-strain curves in material processed to high levels of strain using the MTS model formalism gives another example of how this formalism can be used to give insight into complex deformation paths.

Acknowledgements

Conflicts of Interest

The author declares no conflicts of interest regarding the publication of this paper.

References

[1] Follansbee, P.S. (2014) On the Definition of State Variables for an Internal State Va-riable Constitutive Model Describing Metal Deformation. *Materials Sciences*

and Application, **5**, 603-609. http://dx.doi.org/10.4236/msa.2014.58062

[2] Kocks, U.F., Argon, A.S. and Ashby, M.F. (1975) Thermodynamics and Kinetics of Slip. In: Chalmers, B., Christian, J.W. and Massalski, T.B., Eds., *Progress in Materials Science*, Vol. 19, Pergamon Press, Oxford.

[3] Follansbee, P.S. (2014) Fundamentals of Strength: Principles, Experiment, and Applications of an Internal State Variable Constitutive Formulation. Wiley, Hoboken. https://doi.org/10.1002/9781118808412

[4] Follansbee, P.S. and Kocks, U.F. (1988) A Constitutive Description of the Defor-mation of Copper Based on the Use of the Mechanical Threshold Stress as an Internal State Variable. *Acta Metallurgica*, **36**, 81-93. https://doi.org/10.1016/0001-6160(88)90030-2

[5] Varshni, Y.P. (1970) Temperature Dependence of the Elastic Constants. *Physical Review B*, **2**, 3952-3958. https://doi.org/10.1103/PhysRevB.2.3952

[6] Meyers, M.A., Mishra, A. and Benson, D.J. (2006) Mechanical Properties of Nano-Crystalline Materials. *Progress in Materials Science*, **51**, 427-556. https://doi.org/10.1016/j.pmatsci.2005.08.003

[7] Kumar, K.A., Van Swygenhoven, H. and Suresh, S. (2003) Mechanical Behavior of Nanocrystalline Metals and Alloys. *Acta Materialia*, **51**, 5743-5774. https://doi.org/10.1016/j.actamat.2003.08.032

[8] Mecking, H. and Kocks, U.F. (1981) Kinetics of Flow and Strain-Hardening. *Acta Metallurgica*, **29**, 1865-1875. https://doi.org/10.1016/0001-6160(81)90112-7

[9] Voce, E. (1948) The Relationship Between Stress and Strain for Homogeneous De-formation. *Journal of the Institute of Metals*, **74**, 537-562.

[10] Alberti, J.M.G. (1984) Large Plastic Deformations in Polycrystalline Cu and Al at Low Temperatures. PhD Thesis, University Navarra, Pamplona.

[11] Kocks, U.F., Stout, M.G. and Rollett, A.D. (1988) Influence of Texture on Strain Hardening. *Proceedings of the* 8*th International Conference on The Strength of Metals and Alloys Tampere*, Finland, 26 August 1988, 25-34. https://doi.org/10.1016/B978-0-08-034804-9.50008-5

[12] Rollett, A.D. and Kocks, U.F. (1993) A Review of the Stages of Work Hardening, *Solid State Phenomena*, **35**-**36**, 1-18. https://doi.org/10.4028/www.scientific.net/SSP.35-36.1

[13] Kocks, U.F. (1976) Laws for Work-Hardening and Low-Temperature Creep. *ASME Journal of Engineering Materials and Technology*, **98**, 76-85. https://doi.org/10.1115/1.3443340

[14] Torre, D.F.H., Pereloma, E.V. and Davies, C.H.J. (2006) Strain Hardening Behaviour and Deformation Kinetics of Cu Deformed by Equal Channel Angular Extrusion from 1 to 16 Passes. *Acta Materialia*, **54**, 1135-1146. https://doi.org/10.1007/s10853-008-2903-8

[15] Zhang, Y., Wang, J.T. and Cheng, C. (2008) Stored Energy and Recrystallization Temperature in High Purity Copper after Equal Channel Angular Pressing. *Journal of Materials Science*, **43**, 7326-7330. https://doi.org/10.1007/s10853-008-2903-8

[16] Miller, M.P. and McDowell, D.L. (1993) The Effect of Stress-State on the Large Strain Inelastic Deformation Behavior of 304L Stainless Steel. *ASME Journal of Engineering Materials and Technology*, **118**, 28-36. https://doi.org/10.1115/1.2805930